AUTHOR(S): ZOU, G., LIU, B., GUO, J., ZHANG, Q., FERNANDEZ, C. and PENG, Q.

TITLE: Synthesis of nanoflower-shaped MXene derivative with unexpected catalytic activity for dehydrogenation of sodium alanates.

YEAR: 2017

Publisher citation: ZOU, G., LIU, B., GUO, J., ZHANG, Q., FERNANDEZ, C. and PENG, Q. 2017. Synthesis of nanoflower-shaped MXene derivative with unexpected catalytic activity for dehydrogenation of sodium alanates. ACS applied materials and interfaces [online], 9(8), pages 7611-7618. Available from: https://doi.org/10.1021/acsami.6b13973

OpenAIR citation: ZOU, G., LIU, B., GUO, J., ZHANG, Q., FERNANDEZ, C. and PENG, Q. 2017. Synthesis of nanoflower-shaped MXene derivative with unexpected catalytic activity for dehydrogenation of sodium alanates. ACS applied materials and interfaces, 9(8), pages 7611-7618. Held on OpenAIR [online]. Available from: https://openair.rgu.ac.uk

ACS APPLIED MATERIALS & INTERFACES

Research Article

www.acsami.org

Synthesis of Nanoflower-Shaped MXene Derivative with Unexpected Catalytic Activity for Dehydrogenation of Sodium Alanates

Guodong Zou,[†] Baozhong Liu,[†,‡] Jianxin Guo,[†,§] Qingrui Zhang,[*,∥] Carlos Fernandez,[⊥] and Qiuming Peng[*,†]

[†]State Key Laboratory of Metastable Materials Science and Technology, and [∥]Hebei Key Laboratory of Applied Chemistry, School of Environmental and Chemical Engineering, Yanshan University, Qinhuangdao 066004, P.R. China

[‡]School of Materials Science and Engineering, Henan Polytechnic University, Jiaozuo 454000, P.R. China

[§]Hebei Provincial Key Lab of Optoelectronic Information Materials, College of Physics Science and Technology, Hebei University, Baoding 071002, P.R. China

[⊥]School of Pharmacy and Life Sciences, Rober Gordon University, Aberdeen, AB107GJ, United Kingdom

Supporting Information

ABSTRACT: Surface group modification and functionalization of two-dimensional materials in many cases are deemed as effective approaches to achieve some distinctive properties. Herein, we present a new nanoflower-shaped TiO_2/C composite which was synthesized by in situ alcoholysis of two-dimensional layered MXene ($Ti_3C_2(OH_xF_{1-x})_2$) in a dilute HF solution (0.5 wt %) for the first time. Furthermore, it is demonstrated that it bestows a strong catalytic activity for the dehydrogenation of $NaAlH_4$. The results show that the $NaAlH_4$ containing 10 wt % $A_{0.9}R_{0.1}$−TiO_2/C (containing 90% anatase TiO_2 and 10% rutile TiO_2) composite merely took ∼85 min to reach a stable and maximum dehydrogenation capacity of ∼3.08 wt % at 100 °C, and it maintains stable after ten cycles, which is the best Ti-based catalyst for the dehydrogenation of $NaAlH_4$ reported so far. Theoretical calculation confirms that this C-doping TiO_2 crystals remarkably decreases desorption energy barrier of Al−H bonding in $NaAlH_4$, accelerating the breakdown of Al−H bonding. This finding raises the potential for development and application of new fuel cells.

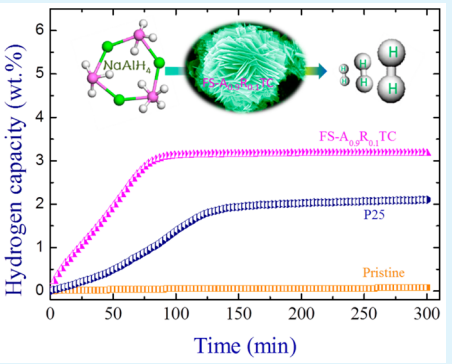

KEYWORDS: *MXene, catalytic properties, two dimension, phase transformation, dehydrogenation*

1. INTRODUCTION

Fuel cells are regarded as a potential alternative energy to decrease dependence on fossil fuels,[1] whereas until now it still meets some challenges, such as an absence of suitable hydrogen storage, low-cost system to be used. Recently, significant efforts have been devoted to developing solid-state metallic systems for hydrogen storage in viewpoints of safety and reversibility.[2] The $NaAlH_4$ compound, which was pioneered by Bogdanovic et al.,[3,4] has been deemed a promising candidate for fuel cells because of its high reversible hydrogen storage capacity and optimal thermodynamic stability for hydrogen storage at medium temperatures, though its maximum gravimetric capacity is ∼4.5%.[4] The main hurdles of $NaAlH_4$ applications lie in its slow kinetics and poor reversibility.[3] Therefore, some methods, such as catalyst doping,[5] nanoengineering,[6,7] and reactant destabilization, have been performed to enhance its hydrogen storage properties. Among these methods, the catalysts are more attractive in terms of industrial viewpoints. Figure 1 shows the combination of dehydrogenation properties of $NaAlH_4$ accompanying different catalysts.[3,4,6−26] Compared to other catalysts, the Ti-based catalyst is the most possible counterpart to improve dehydrogenation properties in the temperature range of 150−250 °C since the barrier mainly originates from kinetics rather than thermodynamics.[2,27−29] Unfortunately, the low cycle stability and relatively high dehydrogenation temperature slow its application rhythm although some nanocrystalline TiO_2 supported on nanoporous carbon[30] and Ti−C ordered mesoporous carbon[31] provide high dehydriding performances but low hydrogen capacity. Hence the applications of $NaAlH_4$ for proton exchange membrane (PEM) fuel cells at low temperatures (∼100 °C) are still severely restricted.

Basically, the formation of Ti−O, Ti−F, and Ti−C bonds is of particular benefit to develop some new catalysts for dehydrogenation.[3,4,6−26] Coincidentally, the recently developed MXene ($Ti_3C_2(OH_xF_{1-x})_2$) materials contain a larger amount of such bonds.[32−34] The external surface of MXene after Al removal is terminated by OH or F groups by forming Ti−OH or Ti−F bonds.[35] Meanwhile, the MXene can also change to TiO_2 structure by heat decomposition or hydrothermal

Received: December 3, 2016
Accepted: February 13, 2017
Published: February 14, 2017

DOI: 10.1021/acsami.6b13973
ACS Appl. Mater. Interfaces XXXX, XXX, XXX−XXX

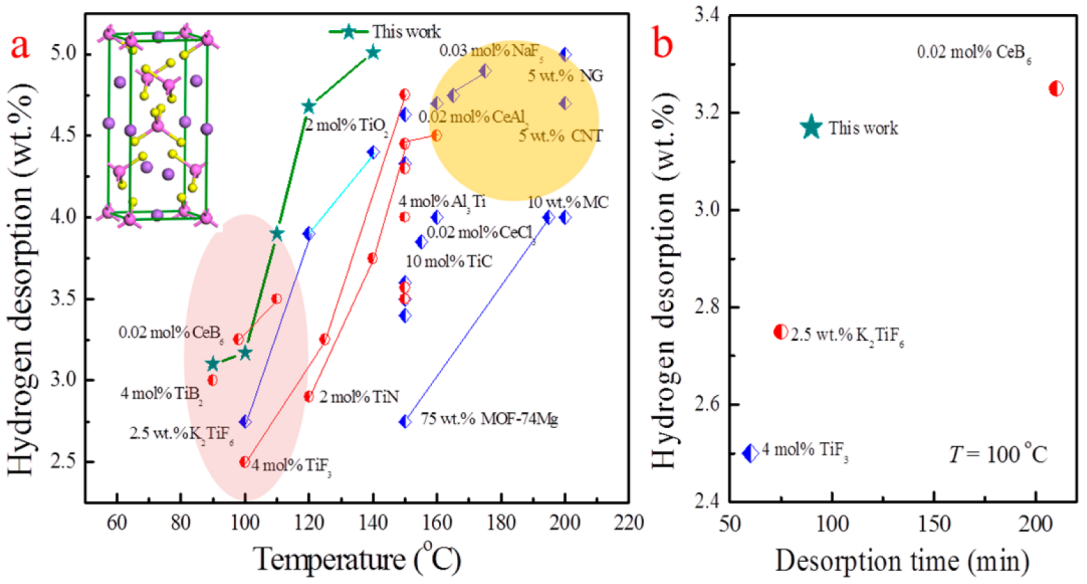

Figure 1. Optimization of the dehydrogenation catayst profile for $NaAlH_4$. (a) Property space for dehydrogenation desorption versus temperature. The inset correponds to the crystal stucture of $NaAlH_4$. The pink ellipsoid and the yellow circle represent the range for PEC at low temperatures and the high dehydrogenation amount at elevated temperatures. The different colors are used to distinguish the test samples which were prepared by using different raws. The red signs represent the raws of NaH and Al, while the blue signs correspond to the raw of $NaAlH_4$. The connections mean the same samples. (b) Property space for hydrogen desorption versus desorption time at 100 °C. The data in these figures are compared with other catalysts in the published literature, showing the signifcant improvement in the dehydrogenation amount in combination with the kinetics.

reaction,[36−38] which can be used as lithium ion batteries electrodes or adsorbents.[39,40] Both of them provide some prerequisites to design such new catalysts.

Noteworthy, it is confirmed that not only do phase transformations occur on the surface groups of MXene in the different aqueous solvents[39] but also the whole MXene structure can be continuously decomposed by varying HF concentrations.[41] In addition, the presence of F groups on MXene surface significantly determines the growth of TiO_2 crystallographic planes. Therefore, it is expected to prepare some new MXene derivatives with some distinctive chemical properties. Herein, we achieved a new $A_{0.9}R_{0.1}$-TiO_2/C nanocomposite by alcoholysis reaction of MXene in solutions containing dilute HF concentration of 0.5 wt % for the first time. Attractively, this nanoflower-shaped $A_{0.9}R_{0.1}$−TiO_2/C composite (FS-$A_{0.9}R_{0.1}$TC, containing 90% anatase TiO_2 and 10% rutile TiO_2) bestows unexpected high catalytic activity for the dehydrogenation of $NaAlH_4$. It remarkably improves dehydrogenation capacity, kinetics, and stability relative to the previously reported catalysts (Figure 1). To the best of our knowledge, this is the first time to report the synthesis of nanoflower-shaped 2D-MXene composite. This composite was successfully evaluated as a catalyst toward the dehydrogenation of $NaAlH_4$. Furthermore, the low dehydrogenation temperature, high cycle stability, and simple procedure on large scale are especially desirable for the development of new PEM fuel cells.

2. MATERIALS AND METHODS

2.1. Preparation of Different MXene Derivative Composites. The processing of MXene has been reported in detail in our previous results.[35] The flower-shaped (A-TiO_2 + R-TiO_2)/C composite was achieved by solvent-thermal decomposition of MXene. The solvent compositions were shown in Table S1. The mixture (0.5 g of MXene, 15 mL of ethylene glycol (EG), 25 mL of isopropyl alcohol (IPA), and 0.5 mL of HF) was continuously sonicated for 15 min and stirred for 3 h at room temperature. Then the above solution was added into a Teflon autoclave and heated at 200−250 °C for 8−48 h in an electric blast drying oven. After the reaction was completed, the gray precipitate on the bottom was moved to a 50 mL centrifuge tube and centrifuged at 3600 rpm with deionized water and ethyl alcohol at least four times (20 min for each time) to remove unreacted solution. After removal of the supernatant, the sediment was dried at 80 °C under vacuum for 24 h to obtain the final flower-shaped (A-TiO_2 + R-TiO_2)/C composite (FS-$A_{0.9}RT_{0.1}$TC). The detail concentration ratio was obtained, dependent on the following Rietveld refinement.

2.2. Hydriding/Dehydriding Measurements. $NaAlH_4$ (high purity, Sigma-Aldrich, St. Louis) samples with different additives were treated by ball milling (QM-3MP4, Nanjing) under an Ar atmosphere at 500 rpm for 12 h. All preparation processes were done in a glove box with the protection of pure argon gas (H_2O, O less than 1 ppm). The weight concentration of all catalysts remained at 10 wt % to compare their catalytic properties.

A lab-built Sievert's apparatus was used to measure the hydrogen sorption. The detailed testing process and mechanism have been reported in our previous results.[42] Basically, all the steps were prepared under Ar atmosphere. Approximately 0.3 g of sample was used for hydrogen sorption. Sieverts methods were used to study the effect of the temperature on the desorbed amount of hydrogen (temperature-programmed desorption: TPD). The temperature increased in the range of 25−200 °C at a rate of 2 °C/min. The initial hydrogen pressure of the channel was 0.001 MPa. The heating rate is ∼15 °C/min. During the hydrogenation/dehydrogenation cycles, the sample was hydrogenated at 120 °C under the hydrogen pressure of 10 MPa for 6 h.

2.3. Analysis and Characterization. The X-ray diffraction (XRD, Rigaku D/MAX-2005/PC) results were attained using Cu Kα radiation (λ = 1.5406 Å) at a voltage of 40 kV with a step-scanning speed of 2°/min. The testing results were analyzed in terms of Rietveld refinement (the software Fullprof).

The morphologies were characterized by a field emission scanning electron microscopy (FESEM, Hitachi S4800, Japan) and the transmission electron microscopy (TEM) and high-resolution transmission electron microscopy (HRTEM, JEOL JEM2010) at accelerating voltage of 200 kV. The bonding composition was analyzed by X-ray photoelectron spectroscopy (XPS, UlVAC-PHI model 5000 Versa probe), and the peaks were fitted by using a curve-

DOI: 10.1021/acsami.6b13973
ACS Appl. Mater. Interfaces XXXX, XXX, XXX−XXX

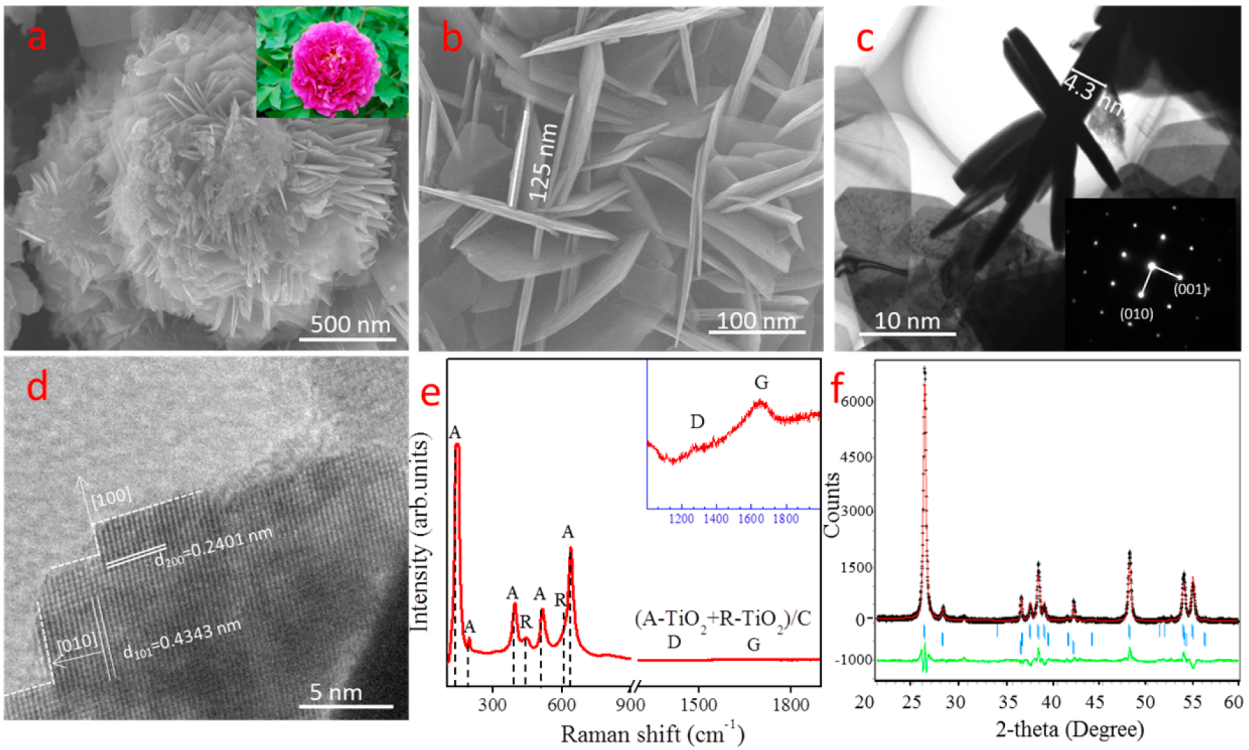

Figure 2. Microstructure characteristics. (a) A representative SEM graph of FS-$A_{0.9}R_{0.1}$-TiO_2/C. The inset is the peony morphology. (b) High-magnification graph of petals. (c) Typical TEM graph of FS-$A_{0.9}R_{0.1}$-TiO_2/C. The thin sheet and fine rod correspond to A-TiO_2 and R-TiO_2, respectively. The inset represents the SAED of A-TiO_2 sheet. (d) HRTEM graph of A-TiO_2 sheet. (e) Raman spectroscopy of FS-$A_{0.9}R_{0.1}$-TiO_2/C. (f) Rietveld structure refinement of FS-$A_{0.9}R_{0.1}$-TiO_2/C.

fitting program (XPS-peak4.1) The reference C 1s at 284.2 eV was used to calibrate the binding energies.

2.4. Computational Details. The calculations were finished with the Vienna ab initio Simulation Package (VASP) code in terms of the density functional theory (DFT).[43] The function and approximation have been introduced in previous results.[44] Briefly, the cutoff energy was 520 eV. A 3 × 3 × 1 supercell of A-TiO_2 and A-TiO_2/C and a 3 × 3 × 1 supercell of R-TiO_2 and R-TiO_2/C were used, respectively. The smearing value, which was determined by a Methfessel-Paxton smearing scheme,[45] was 0.1 eV. The DFT-D3 method[46] was involved to calculate the van der Waals (vdW) interaction. A vacuum space was 15 Å, and it can effectively eliminate the effect between sheets.

3. RESULTS AND DISCUSSION

3.1. Microstructure Characteristics. Typically, Ti_3AlC_2 powders were mixed with a solution of LiF and 6 M HCl and heated at 60 °C for 48 h. After reaction, the samples were separated and washed to obtain the reaction products. A representative exfoliated morphology of layered MXene (Supporting Information, Figure S1a) was observed by FESEM. The gap width and layer thickness are ~100 ± 50 nm and ~25 nm, respectively. It is similar to the results by etching in 40% HF solution.[35] Note that the TiC peaks (~3.9 wt %) which formed during hot-pressed sintering maintain invariable.[35]

A hierarchical nanoflower-shaped morphology has first been achieved by alcohol-thermal decomposition of MXene in a mixing solution of EG, 0.5 mL of HF solution, and IPA (Figure 2a, Table S1). EG and IPA are added to strengthen the F adsorption on the surface. The average size of nanoflower-shaped structure with a hierarchical structure is ~1.25 μm. The high-magnification image reveals that the petals are mainly composed of some intercrossed sheets with a width of ~125 nm and a thickness of ~4.3 nm (Figure S1). The TEM images of separated flowers (Figure 2c,d) present the high-resolution crystal structure of the petals. The selected area electron diffraction (SAED) can be assigned into diffraction spots of the [100] zone axis. Examination of individual nanosheet with high-resolution TEM shows that the petals are completely crystalline along their entire lengths. Lattice figures with interplanar spacing, d_{101} = 4.34 ± 0.02 Å and d_{200} = 2.40 ± 0.02 Å, are evidently confirmed, and they correspond to anatase TiO_2 (A-TiO_2) phase.[46,47] In addition, Raman spectra (Figure 2e) and X-ray diffraction patterns (XRD, Figure 2f) demonstrate that the flower-shaped sample mainly consists of a large number of A-TiO_2, a little C (graphene type[11]) and rutile TiO_2 (R-TiO_2). The impurity of TiC (~3.1 wt %) comes from hot-pressed sintering. The ratio of chemical composition between A-TiO_2 and R-TiO_2 is ~9.19 in terms of Rietveld refinement (Figure S2). The C element comes from the decomposition of C layer in MXene, which is consistent with the results reported by thermal decomposition or hydrothermal reaction.[48,49] According to the aforementioned results, this new sample can be abbreviated as a FS-$A_{0.9}R_{0.1}$TC (Table S1).

To elucidate the formation process of FS-$A_{0.9}R_{0.1}$TC, the FESEM graphs (Figure S1) and XRD patterns (Figure S3a) after reacting for different time intervals were performed. At the initial reaction stage (4 h), the whole layer structure remains and the peak of 9° is observed. However, apart from MXene peaks, there are some new peaks detected based on the XRD results. Some $TiOF_2$ peaks are detected. As incubation time is further increased (over 8 h), the peaks of $TiOF_2$ become weak, suggesting the occurrence of phase transformation. This trend has also been confirmed by XPS investigation (Figure 3). The distinguished Ti $2p_{3/2}$ and Ti $2p_{1/2}$ peaks within the primitive

DOI: 10.1021/acsami.6b13973
ACS Appl. Mater. Interfaces XXXX, XXX, XXX−XXX

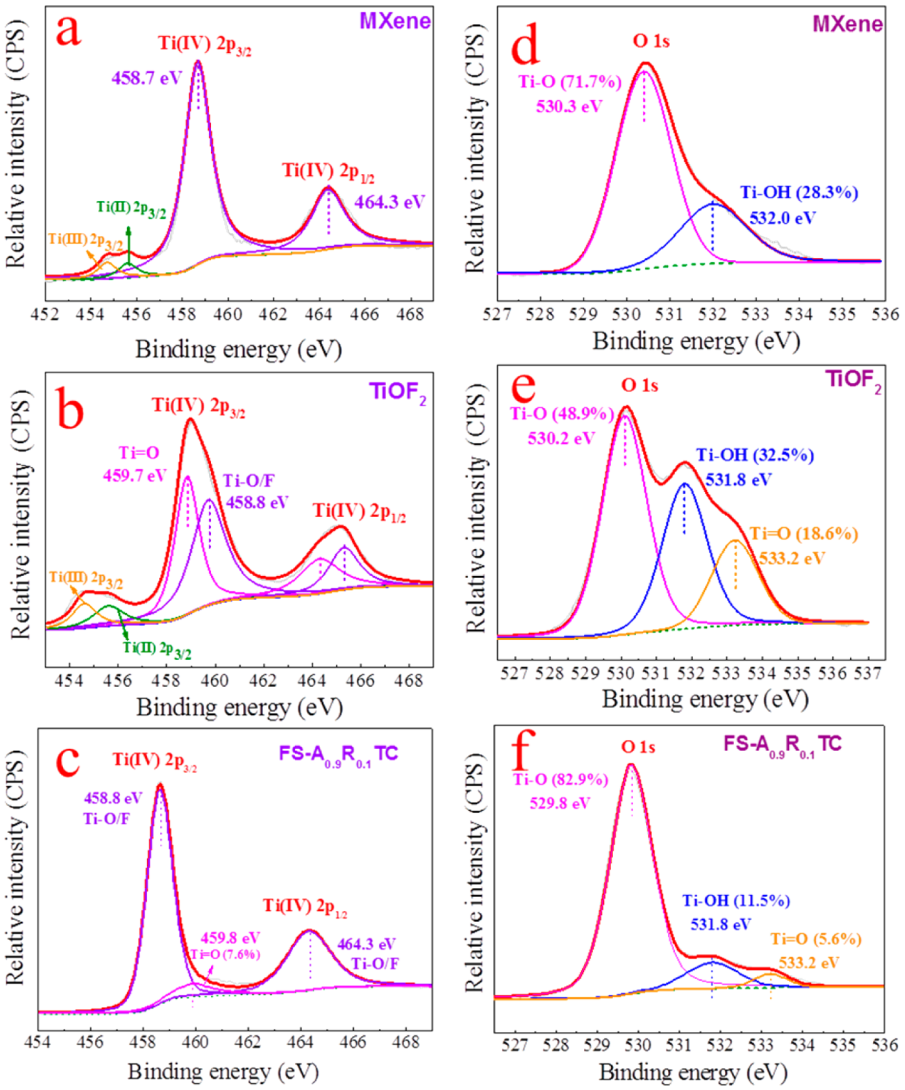

Figure 3. Variation of different elemental states. (a) Ti 2p spectra of MXene. (b) Ti 2p spectra of $TiOF_2$ (4 h). (c) Ti 2p spectra of FS-$A_{0.9}R_{0.1}$TC (4 h). (d) O 1s spectra of MXene. (e) O 1s spectra of $TiOF_2$(4 h). (f) O 1s spectra of FS-$A_{0.9}R_{0.1}$TC (4 h).

MXene were located at ~458.7 and ~464.3 eV, respectively, which corresponded to Ti(IV)−O/F species (Figure 3a). Meanwhile, another broad peak ranging from approximately 452.0 to 456.5 eV can be ascribed to the low-valence Ti sources, that is, Ti(II) $2p_{3/2}$ (455.8 eV) and Ti(III) $2p_{3/2}$ (454.7 eV), respectively. Interestingly, a new kind of Ti 2p was observed after thermal reaction for 4 h. The corresponding full width at half-maximum (fwhm) of Ti(IV) 2p widened, in which a new Ti(IV) species emerged at approximately 459.7 eV for Ti(IV) $2p_{3/2}$ and 465.2 eV for Ti(IV) $2p_{1/2}$, respectively (Figure 3b), which might be attributed to the formation of $TiOF_2$ intermediate (Ti(IV)═O).[30,39] Finally, the majority of $TiOF_2$ species and low-valence Ti sources transformed into the Ti(IV)−O composition after reaction for 24 h (Figure 3c).

Additionally, the O 1s peaks also revealed a similar conversion process. The representative O 1s peak was composed of the Ti−O (~530.3 eV) and Ti−OH (~532.0 eV) on the bare MXene material with the peak area of 71.7% and 28.3%, correspondingly (Figure 3d). Comparatively, a new O 1s peak was detected (Figure 3e) at the initial reaction stage (4 h), which was related to the formation of double-bond oxygen in $TiOF_2$ intermediate product. The composition ratio of Ti−O, Ti−OH, and Ti═O was approximately 49.8:32.5:18.6%, indicating that the possible species transformed from Ti−O and Ti−OH to intermediate $TiOF_2$, which was consistent with the variation of the Ti 2p spectrum and XRD analysis. Therefore, the reaction process can be shown as follows:

$$Ti_3C_2(OH_{0.8}F_{1.2})_2 \xrightarrow{EG,HF,IPA,<4h} TiOF_2 + C \xrightarrow{\geq 8h} TiO_2/C \quad (1)$$

The width of nanosheet increases with the incubating time at the beginning of the decomposition process and then it remains a constant of ~170 nm. In contrast, the similar trend is also confirmed for the percentage of the (001) plane (Figure S3b). The maximum fraction value of the (001) plane is ~62%.

3.2. Dehydrogenation Properties. To probe potential applications in dehydrogenation catalysts of FS-$A_{0.9}R_{0.1}$TC nanocomposite, the hydrogen desorption properties of the $NaAlH_4$ including 10 wt % samples were evaluated by temperature-programmed desorption (TPD) via volumetric release.[31] The pristine MXene and commercial TiC (99.5%), and P25 (99.9%, containing 85.48 wt % A-TiO_2 and 14.52 wt % R-TiO_2), were involved as the references. All references and the

DOI: 10.1021/acsami.6b13973
ACS Appl. Mater. Interfaces XXXX, XXX, XXX−XXX

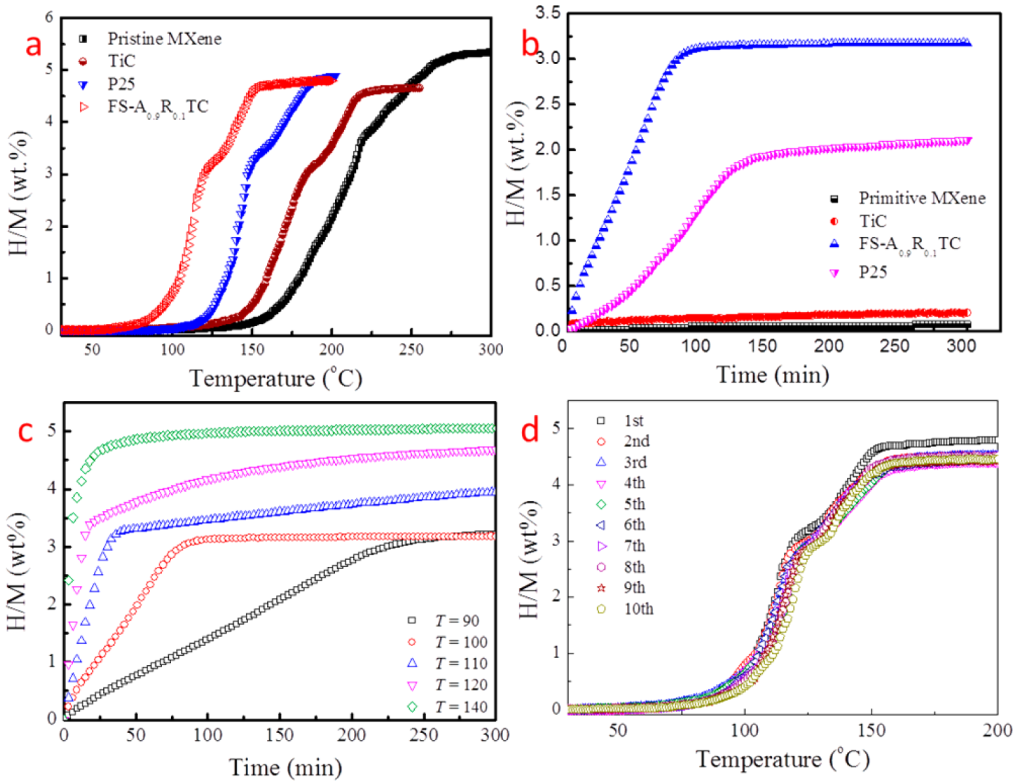

Figure 4. Dehydrogenation properties of MXene derivatives. (a) TPD curves of $NaAlH_4$ with different additives. (b) Isothermal dehydrogenation curves of $NaAlH_4$ with different additives at 100 °C (10 wt % catalyst). (c) Isothermal dehydrogenation curves of $NaAlH_4$ with FS-$A_{0.9}R_{0.1}$TC at different temperatures (10 wt % catalyst). (d) TPD curves of $NaAlH_4$ with FS-$A_{0.9}R_{0.1}$TC at different cycles.

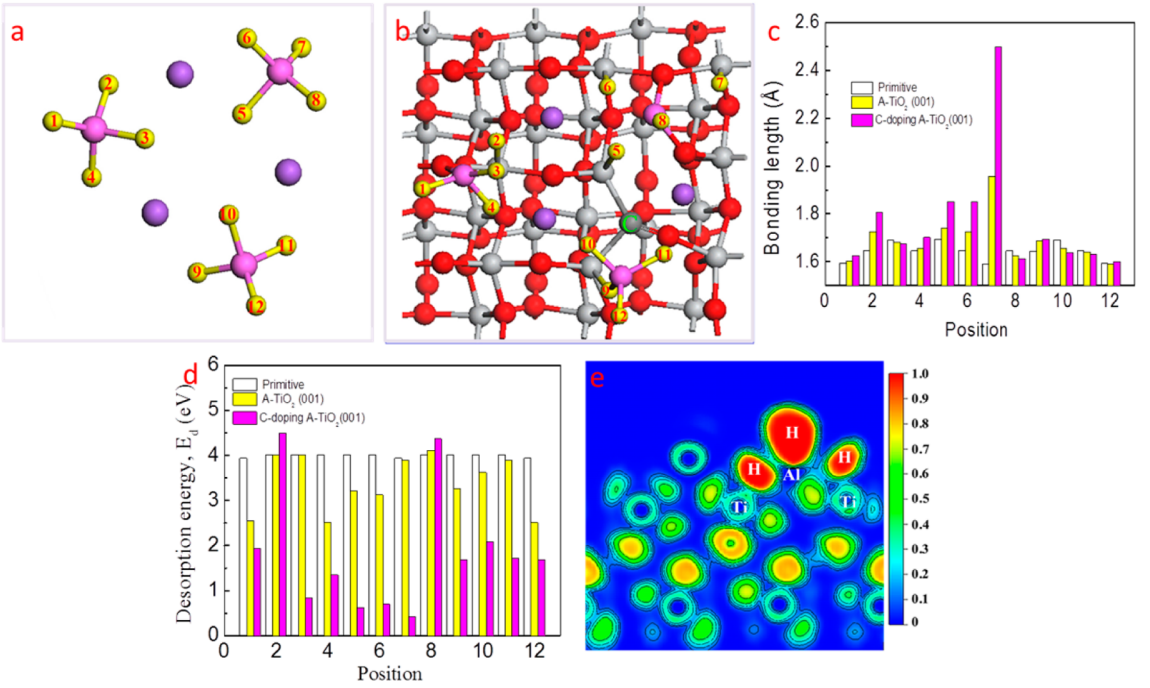

Figure 5. Microstructure variation. (a) Molecular structure of $(NaAlH_4)_3$ clusters. (b) Structure of $(NaAlH_4)_3$ clusters and C-doping A-TiO_2 (001). (c) The lengths of different Al−H bonding in $(NaAlH_4)_3$ clusters, $(NaAlH_4)_3$ /A-TiO_2 (001), and $(NaAlH_4)_3$ /C-doping A-TiO_2 (001). (d) The desorption energy of different H atoms in $(NaAlH_4)_3$ clusters, $(NaAlH_4)_3$/A-TiO_2 (001), and $(NaAlH_4)_3$/C-doping A-TiO_2 (001). (e) ELF of $(NaAlH_4)_3$/C-doping A-TiO_2 (001).

samples have a similar size of 1−2 μm. The typical two-step reactions relative to the decompositions of AlH_4^- and AlH_6^{3-} occurred during all dehydrogenation procedures[3,50] (Figure 4a). All additions decrease the dehydrogenation temperature of $NaAlH_4$ due to the presence of Ti−O, Ti−F, or Ti−C bonds. Attractively, the FS-$A_{0.9}R_{0.1}$TC sample shows the most effective

DOI: 10.1021/acsami.6b13973
ACS Appl. Mater. Interfaces XXXX, XXX, XXX−XXX

performance on the decomposition of AlH_4^- and AlH_6^{3-}. The onset temperature reduces to ~95 °C, which lowers ~60 °C in contrast to the pristine ball-milled $NaAlH_4$. Moreover, the final temperatures of the first and second dehydrogenation step change to 122 and 152 °C, respectively, representing 90 and 115 °C declines relative to those of the pristine $NaAlH_4$ sample, correspondingly.

In addition, hydrogen storage materials which release hydrogen at around 100 °C are of particular interest for PEM fuel cells. The isothermal dehydrogenation tests (Figure 4b) show that the FS-$A_{0.9}R_{0.1}$TC improves the decomposition rate of AlH_6^{3-} groups at low temperature. It can release ~3.11 wt % hydrogen in 90 min, which is better than those reported so far[6−20] (Figure 1b). Moreover, it can rapidly release more than 4.6 wt % of hydrogen within 20 min at 140 °C, and almost all 5.05 wt % of hydrogen is desorbed within 250 min at 140 °C (Figure 4c). However, no hydrogen can be desorbed by pure $NaAlH_4$ at 140 °C. More importantly, the dehydrogenation amount of ~3.08 wt % is achieved within 240 min at 90 °C and 85 min at 100 °C at a constant rate. To the best of our knowledge, it is the best one among the Ti-based catalysts for dehydrogenation of $NaAlH_4$. The FS-$A_{0.9}R_{0.1}$TC additive completely decomposes the AlH_6^{3-} at 110 °C for only 35 min, which is a half value of $NaAlH_4$ + 2 mol % nanosized CeB_6[3].

The dehydrogenation curves of $NaAlH_4$ + 10 wt % FS-$A_{0.9}R_{0.1}$TC samples in the first ten cycles (Figure 4d) reveal its excellent cycling stability, in which a little reduction is observed with increasing the cycling numbers. The dehydrogenation amount remains a constant of ~4.5 wt % after the second cycle, which is approximately 95% of that in contrast to the first cycle. More importantly, the dehydrogenation amount maintains relatively constant for even ten cycles.

To understand the improved kinetics, the activation energy (E_a) of two-step dehydrogenation reactions of $NaAlH_4$ + 10 wt % FS-$A_{0.9}R_{0.1}$TC was calculated using the nonisothermal Kissinger methods according to the following equation,[19,22]

$$\frac{\mathrm{d}\ln(\beta/T_\mu^2)}{\mathrm{d}(1/T_\mu)} = \frac{E_a}{R} \tag{2}$$

where β is the heating rate, T_m is the solute temperature for the maximum desorption rate, and R is the gas constant. T_m was obtained using differential scanning calorimetry measurement with the different heating rates (Figure S4a). The induced results (Figure S4b) show that the E_{aAlH4} and E_{aAlH6} are 57.68 and 67.30 kJ/mol, respectively. They are reduced by 36% and 30% compared with those of the pristine $NaAlH_4$,[3,17,51−54] respectively. Compared with similar Ti-based catalysts or other catalysts (Table S3), the values are also very low.

3.3. Catalytic Mechanism. The catalytic behavior of FS-$A_{0.9}R_{0.1}$TC is elucidated by first principle calculations, wherein the $(NaAlH_4)_3$ cluster as a type of the $NaAlH_4$ structure is selected to investigate the procedure[55] (Figure 5a). It is well-known that the dehydrogenation of $NaAlH_4$ is a process controlled by kinetic activation barrier. Thus, the desorption energy (E_d) of H atoms desorbing from $(NaAlH_4)_3$ is regarded as an important parameter to interpret the catalytic mechanism. Taking into account the high concentration of A-TiO_2 and the high activation of {001} plane,[28,32] the model of A-TiO_2 (001) (Figure 5b) has been simplified to investigate their catalytic properties. In addition, taking into account our experimental process, the C element has two possible existence forms, although it is marked as TiO_2/C. One is graphene, which was verified by Raman spectrum (Figure 2e). The other is related to the C-doped TiO_2 (substituting O sites) confirmed by the shifted peaks (Figure S2−3). Owing to the weak catalytic role of graphene on dehydrogenation,[56] only C-doped A-TiO_2 is considered to simplify the calculations.

The desorption energy (E_d) of one H atom desorbing from $(NaAlH_4)_3$ with or without A-TiO_2 (001) surface is defined as the following,[57]

$$E_d = E - E' - \frac{1}{2}E_{H_2} \tag{3}$$

where E and E' are the total energy before and after desorbing H. E_{H_2} is the total energy of the H_2 molecule.

The variation of Al−H bonding length (Figure 5c) shows that the primitive Al−H bonding is ~1.69 Å. However, the majority of Al−H bonding lengths are increased on the surface of A-TiO_2 (001) substrate. The max value (position 7) changes to ~2.05 Å. It shows that the addition of A-TiO_2 is of benefit for the dehydrogenation of $NaAlH_4$. Comparatively, the trend similar to A-TiO_2 is detected in the C-doping A-TiO_2. The main difference between A-TiO_2 and C-doping A-TiO_2 is that the Al−H bond lengthening is further increased with the addition of C-doping A-TiO_2. The max Al−H length (position 7) is ~2.50 Å, which is 1.48 times than that of the primitive one.

The strengthening dehydrogenation roles of $(NaAlH_4)_3$ clusters are achieved in both A-TiO_2 and C-doping A-TiO_2 (Figure 5d). The average E_d value is ~4.00 eV for the primitive $(NaAlH_4)_3$ clusters. Comparatively, the E_d value is reduced to ~3.00 eV with the addition of A-TiO_2. More attractively, this catalytic dehydrogenation is further strengthened by the C-doping A-TiO_2. The majority of activation energies became ~2 eV. Particularly, the E_d values of one-third sites (positions 3, 5, 6, and 7) are below 1 eV (~0.60 eV). It demonstrates that the C-doping A-TiO_2 additive would remarkably accelerate the dehydrogenation of $(NaAlH_4)_3$ clusters.

The valent electron localization function (ELF, Figure 5e) shows that the surface of Ti atoms is covered by the H atoms. Moreover, the H atom separates the bonding between Ti and Al. It reveals that it is prone to forming Ti−H bonding instead of Ti−Al bonding. The formation of Ti−H bonding enlarges the length of Al−H bonding, which makes the bonding of Al−H weak. This process is confirmed by XRD results (Figure S5), in which only the TiH_x compound is detected during the dehydrogenation, independent of the temperatures.

4. CONCLUSIONS

In summary, this investigation presents a simple method to prepare some intriguing stuctures of two-dimensional MXene derivatives. For example, we successfully achieved a unique flower-shaped $A_{0.9}R_{0.1}$-TiO_2/C nanocomposite which contains 90% anatase TiO_2 and 10% rutile TiO_2 thermal alcoholysis reaction of MXene in a dilute HF solution. This unique structure shows unexpected catalytic activity for the dehydrogenation of $NaAlH_4$ at low temperatures owing to the decreased activation energy barriers. The low dehydrogenation temperature, high cycle stability, and simple procedure on large scale are especially desirable for the development of new PEM fuel cells.

DOI: 10.1021/acsami.6b13973
ACS Appl. Mater. Interfaces XXXX, XXX, XXX−XXX

■ ASSOCIATED CONTENT

Supporting Information

The Supporting Information is available free of charge on the ACS Publications website at DOI: 10.1021/acsami.6b13973.

Experimental details on morphology and phase composition, activation energy test, and comparative data (PDF)

■ AUTHOR INFORMATION

Corresponding Authors

*E-mail: zhangqr@ysu.edu.cn.

*E-mail: pengqiuming@gmail.com.

ORCID

Qiuming Peng: 0000-0002-3053-7066

Author Contributions

Guodong Zhou and Baozhong Liu contributed equally to this work and should be considered cofirst authors.

Notes

The authors declare no competing financial interest.

■ ACKNOWLEDGMENTS

We acknowledge the financial support of NSFC (No. 51422105, 51671080, 51471065) and NSF of Hebei (No. E2015203404). We also are thankful for the help of High-Performance Computing Platform of Hebei University for some computation supports with a "Molecule Aggregated Structure" workstation.

■ REFERENCES

(1) Chong, L.; Zou, J.; Zeng, X.; Ding, W. Mechanisms of Reversible Hydrogen Storage in $NaBH_4$ through NdF_3 Addition. *J. Mater. Chem. A* **2013**, *1*, 3983−3991.

(2) Michel, K.; Ozolins, V. Theory of Mass Transport in Sodium Alanate. *J. Mater. Chem. A* **2014**, *2*, 4438−4448.

(3) Bogdanović, B.; Schwickardi, M. Ti-Doped Alkali Metal Aluminium Hydrides as Potential Novel Reversible Hydrogen Storage Materials. *J. Alloys Compd.* **1997**, *253*−*254*, 1−9.

(4) Bogdanović, B.; Brand, R. A.; Marjanović, A.; Schwickardi, M.; Tölle, J. Metal-Doped Sodium Aluminium Hydrides as Potential New Hydrogen Storage Materials. *J. Alloys Compd.* **2000**, *302*, 36−58.

(5) Xia, Y.; Yang, Z.; Zhu, Y. Porous Carbon-Based Materials for Hydrogen Storage: Advancement and Challenges. *J. Mater. Chem. A* **2013**, *1*, 9365−9381.

(6) Kumar, L.; Rao, C.; Viswanathan, B. Catalytic Effects of Nitrogen-Doped Graphene and Carbon Nanotube Additives on Hydrogen Storage Properties of Sodium Alanate. *J. Mater. Chem. A* **2013**, *1*, 3355−3361.

(7) Fan, X.; Xiao, X.; Shao, J.; Zhang, L.; Li, S.; Ge, H.; Wang, Q.; Chen, L. Size Effect on Hydrogen Storage Properties of $NaAlH_4$ Confined in Uniform Porous Carbons. *Nano Energy* **2013**, *2*, 995−1003.

(8) Stavila, V.; Bhakta, R.; Alam, T.; Majzoub, E.; Allendorf, M. Reversible Hydrogen Storage by $NaAlH_4$ Confined within a Titanium-Functionalized MOF-74(Mg) Nanoreactor. *ACS Nano* **2012**, *6*, 9807−9817.

(9) Rafi-ud-din; Xuanhui, Q.; Ping, L.; Zhang, L.; Qi, W.; Iqbal, M. Z.; Rafique, M.; Farooq, M.; Islam-ud-din. Superior Catalytic Effects of Nb_2O_5, TiO_2, and Cr_2O_3 Nanoparticles in Improving the Hydrogen Sorption Properties of $NaAlH_4$. *J. Phys. Chem. C* **2012**, *116*, 11924−11938.

(10) Li, L.; Qiu, F.; Wang, Y.; Wang, Y.; Liu, G.; Yan, C.; An, C.; Xu, Y.; Song, D.; Jiao, L.; Yuan, H. Crystalline TiB_2: An Efficient Catalyst for Synthesis and Hydrogen Desorption/Absorption Performances of $NaAlH_4$ System. *J. Mater. Chem.* **2012**, *22*, 3127−3132.

(11) Li, L.; Qiu, F.; Wang, Y.; Liu, G.; Xu, Y.; An, C.; Wang, Y.; Jiao, L.; Yuan, H. Tin Catalyst for the Reversible Hydrogen Storage Performance of Sodium Alanate System. *J. Mater. Chem.* **2012**, *22*, 13782−13787.

(12) Hu, J.; Ren, S.; Witter, R.; Fichtner, M. Catalytic Influence of Various Cerium Precursors on the Hydrogen Sorption Properties of $NaAlH_4$. *Adv. Energy Mater.* **2012**, *2*, 560−568.

(13) Mao, J.; Guo, Z.; Liu, H. Improved Hydrogen Sorption Performance of NbF_5-Catalysed $NaAlH_4$. *Int. J. Hydrogen Energy* **2011**, *36*, 14503−14511.

(14) Liu, Y.; Liang, C.; Zhou, H.; Gao, M.; Pan, H.; Wang, Q. A Novel Catalyst Precursor K_2TiF_6 with Remarkable Synergetic Effects of K, Ti and F Together on Reversible Hydrogen Storage of $NaAlH_4$. *Chem. Commun.* **2011**, *47*, 1740−1742.

(15) Fan, X.; Xiao, X.; Chen, L.; Li, S.; Ge, H.; Wang, Q. Enhanced Hydriding−Dehydriding Performance of $CeAl_2$-Doped $NaAlH_4$ and the Evolvement of Ce-Containing Species in the Cycling. *J. Phys. Chem. C* **2011**, *115*, 2537−2543.

(16) Pukazhselvan, D.; Hudson, M.; Sinha, A.; Srivastava, O. Studies on Metal Oxide Nanoparticles Catalyzed Sodium Aluminum Hydride. *Energy* **2010**, *35*, 5037−5042.

(17) Xueping, Z.; Shenglin, L.; Donglin, L. The Effect of Additives on the Hydrogen Storage Properties of $NaAlH_4$. *Int. J. Hydrogen Energy* **2009**, *34*, 2701−2704.

(18) Xiao, X.; Chen, L.; Fan, X.; Wang, X.; Chen, C.; Lei, Y.; Wang, Q. Direct Synthesis of Nanocrystalline $NaAlH_4$ Complex Hydride for Hydrogen Storage. *Appl. Phys. Lett.* **2009**, *94*, 041907.

(19) Xiao, X.; Fan, X.; Yu, K.; Li, S.; Chen, C.; Wang, Q.; Chen, L. Catalytic Mechanism of New TiC-Doped Sodium Alanate for Hydrogen Storage. *J. Phys. Chem. C* **2009**, *113*, 20745−20751.

(20) Bhakta, R.; Herberg, J.; Jacobs, B.; Highley, A.; Behrens, R.; Ockwig, N.; Greathouse, J.; Allendorf, M. Metal−Organic Frameworks as Templates for Nanoscale $NaAlH_4$. *J. Am. Chem. Soc.* **2009**, *131*, 13198−13199.

(21) Berseth, P.; Harter, A.; Zidan, R.; Blomqvist, A.; Araújo, C.; Scheicher, R.; Ahuja, R.; Jena, P. Carbon Nanomaterials as Catalysts for Hydrogen Uptake and Release in $NaAlH_4$. *Nano Lett.* **2009**, *9*, 1501−1505.

(22) Lee, G.; Shim, J.; Cho, Y.; Lee, K. Improvement in Desorption Kinetics of $NaAlH_4$ Catalyzed with TiO_2 Nanopowder. *Int. J. Hydrogen Energy* **2008**, *33*, 3748−3753.

(23) Lee, G.; Shim, J.; Whan Cho, Y.; Sub Lee, K. Reversible Hydrogen Storage in Catalyzed with Lanthanide Oxides. *Int. J. Hydrogen Energy* **2007**, *32*, 1911−1915.

(24) Kang, X.; Wang, P.; Cheng, H. Improving Hydrogen Storage Performance of $NaAlH_4$ by Novel Two-Step Milling Method. *J. Phys. Chem. C* **2007**, *111*, 4879−4884.

(25) Wang, P.; Kang, X.; Cheng, H. Dependence of H-Storage Performance on Preparation Conditions in TiF_3 Doped $NaAlH_4$. *J. Alloys Compd.* **2006**, *421*, 217−222.

(26) Kang, X.; Wang, P.; Song, X.; Yao, X.; Lu, G.; Cheng, H. Catalytic Effect of Al_3Ti on the Reversible Dehydrogenation of $NaAlH_4$. *J. Alloys Compd.* **2006**, *424*, 365−369.

(27) Wang, Y.; Li, L.; Qiu, F.; An, C.; Wang, Y.; Jiao, L.; Yuan, H. Synergetic Effects of $NaAlH_4$-TiF_3 Co-Additive on Dehydriding Reaction of $Mg(AlH_4)_2$. *J. Energy Chem.* **2014**, *23*, 726−731.

(28) Li, L.; Wang, Y.; Qiu, F.; Wang, Y.; Xu, Y.; An, C.; Jiao, L.; Yuan, H. Reversible Hydrogen Storage Properties of $NaAlH_4$ Enhanced with Tin Catalyst. *J. Alloys Compd.* **2013**, *566*, 137−141.

(29) Lin, S.; Yang, J.; Kung, H. Transition Metal-Decorated Activated Carbon Catalysts for Dehydrogenation of $NaAlH_4$. *Int. J. Hydrogen Energy* **2012**, *37*, 2737−2741.

(30) Rafi-ud-din; Xuanhui, Q.; Zahid, G.; Asghar, Z.; Shahzad, M.; Iqbal, M.; Ahmad, E. Improved Hydrogen Storage Performances of MgH_2−$NaAlH_4$ System Catalyzed by TiO_2 Nanoparticles. *J. Alloys Compd.* **2014**, *604*, 317−324.

(31) Zhang, X.; Liu, Y.; Pang, Y.; Gao, M.; Pan, H. Significantly Improved Kinetics, Reversibility and Cycling Stability for Hydrogen

Storage in $NaAlH_4$ with the Ti-Incorporated Metal Organic Framework Mil-125(Ti). *J. Mater. Chem. A* **2014**, *2*, 1847−1854.
(32) Naguib, M.; Kurtoglu, M.; Presser, V.; Lu, J.; Niu, J.; Heon, M.; Hultman, L.; Gogotsi, Y.; Barsoum, M. Two-Dimensional Nanocrystals Produced by Exfoliation of Ti_3AlC_2. *Adv. Mater.* **2011**, *23*, 4248−4253.
(33) Naguib, M.; Come, J.; Dyatkin, B.; Presser, V.; Taberna, P.; Simon, P.; Barsoum, M.; Gogotsi, Y. MXene: A Promising Transition Metal Carbide Anode for Lithium-Ion Batteries. *Electrochem. Commun.* **2012**, *16*, 61−64.
(34) Naguib, M.; Halim, J.; Lu, J.; Cook, K.; Hultman, L.; Gogotsi, Y.; Barsoum, M. New Two-Dimensional Niobium and Vanadium Carbides as Promising Materials for Li-Ion Batteries. *J. Am. Chem. Soc.* **2013**, *135*, 15966−15969.
(35) Peng, Q.; Guo, J.; Zhang, Q.; Xiang, J.; Liu, B.; Zhou, A.; Liu, R.; Tian, Y. Unique Lead Adsorption Behavior of Activated Hydroxyl Group in Two-Dimensional Titanium Carbide. *J. Am. Chem. Soc.* **2014**, *136*, 4113−4116.
(36) Wang, L.; Zhang, H.; Wang, B.; Shen, C.; Zhang, C.; Hu, Q.; Zhou, A.; Liu, B. Synthesis and Electrochemical Performance of $Ti_3C_2T_x$ with Hydrothermal Process. *Electron. Mater. Lett.* **2016**, *12*, 702−710.
(37) Gao, Y.; Wang, L.; Zhou, A.; Li, Z.; Chen, J.; Bala, H.; Hu, Q.; Cao, X. Hydrothermal Synthesis of TiO_2/Ti_3C_2 Nanocomposites with Enhanced Photocatalytic Activity. *Mater. Lett.* **2015**, *150*, 62−64.
(38) Li, Z.; Wang, L.; Sun, D.; Zhang, Y.; Liu, B.; Hu, Q.; Zhou, A. Synthesis and Thermal Stability of Two-Dimensional Carbide MXene Ti_3C_2. *Mater. Sci. Eng., B* **2015**, *191*, 33−40.
(39) Zou, G.; Guo, J.; Peng, Q.; Zhou, A.; Zhang, Q.; Liu, B. Synthesis of Urchin-Like Rutile Titania Carbon Nanocomposites by Iron-Facilitated Phase Transformation of MXene for Environmental Remediation. *J. Mater. Chem. A* **2016**, *4*, 489−499.
(40) Ying, Y.; Liu, Y.; Wang, X.; Mao, Y.; Cao, W.; Hu, P.; Peng, X. Two-Dimensional Titanium Carbide for Efficiently Reductive Removal of Highly Toxic Chromium(VI) from Water. *ACS Appl. Mater. Interfaces* **2015**, *7*, 1795−1803.
(41) Naguib, M.; Mashtalir, O.; Carle, J.; Presser, V.; Lu, J.; Hultman, L.; Gogotsi, Y.; Barsoum, M. Two-Dimensional Transition Metal Carbides. *ACS Nano* **2012**, *6*, 1322−1331.
(42) Fu, H.; Wu, W.; Dou, Y.; Liu, B.; Li, H.; Peng, Q. Hydrogen Diffusion Kinetics and Structural Integrity of Superhigh Pressure Mg-5 wt%Ni Alloys with Dendrite Interface. *J. Power Sources* **2016**, *320*, 212−222.
(43) Kresse, G.; Furthmüller, J. Efficient Iterative Schemes for Ab Initio Total-Energy Calculations Using a Plane-Wave Basis Set. *Phys. Rev. B: Condens. Matter Mater. Phys.* **1996**, *54*, 11169−11186.
(44) Guo, J.; Fu, H.; Zou, G.; Zhang, Q.; Zhang, Z.; Peng, Q. Theoretical Interpretation on Lead Adsorption Behavior of New Two-Dimensional Transition Metal Carbides and Nitrides. *J. Alloys Compd.* **2016**, *684*, 504−509.
(45) Methfessel, M.; Paxton, A. High-Precision Sampling for Brillouin-Zone Integration in Metals. *Phys. Rev. B: Condens. Matter Mater. Phys.* **1989**, *40*, 3616−3621.
(46) Grimme, S.; Ehrlich, S.; Goerigk, L. Effect of the Damping Function in Dispersion Corrected Density Functional Theory. *J. Comput. Chem.* **2011**, *32*, 1456−1465.
(47) Yang, X.; Li, Z.; Sun, C.; Yang, H.; Li, C. Hydrothermal Stability of {001} Faceted Anatase TiO_2. *Chem. Mater.* **2011**, *23*, 3486−3494.
(48) Yang, H.; Sun, C.; Qiao, S.; Zou, J.; Liu, G.; Smith, S.; Cheng, H.; Lu, G. Anatase TiO_2 Single Crystals with a Large Percentage of Reactive Facets. *Nature* **2008**, *453*, 638−641.
(49) Ghassemi, H.; Harlow, W.; Mashtalir, O.; Beidaghi, M.; Lukatskaya, M.; Gogotsi, Y.; Taheri, M. In Situ Environmental Transmission Electron Microscopy Study of Oxidation of Two-Dimensional Ti_3C_2 and Formation of Carbon-Supported TiO_2. *J. Mater. Chem. A* **2014**, *2*, 14339−14343.
(50) Naguib, M.; Mashtalir, O.; Lukatskaya, M.; Dyatkin, B.; Zhang, C.; Presser, V.; Gogotsi, Y.; Barsoum, M. One-Step Synthesis of Nanocrystalline Transition Metal Oxides on Thin Sheets of Disordered Graphitic Carbon by Oxidation of MXenes. *Chem. Commun.* **2014**, *50*, 7420−7423.
(51) Yang, H. G.; Zeng, H. C. Control of Nucleation in Solution Growth of Anatase TiO_2 on Glass Substrate. *J. Phys. Chem. B* **2003**, *107*, 12244−12255.
(52) Sheppard, D.; Jepsen, L.; Jensen, T.; Paskevicius, M.; Buckley, C. New Directions for Hydrogen Storage: Sulphur Destabilised Sodium Aluminium Hydride. *J. Mater. Chem. A* **2013**, *1*, 12775−12781.
(53) Li, H.; Shen, X.; Liu, Y.; Wang, L.; Lei, J.; Zhang, J. Facile Phase Control for Hydrothermal Synthesis of Anatase-Rutile TiO_2 with Enhanced Photocatalytic Activity. *J. Alloys Compd.* **2015**, *646*, 380−386.
(54) Gao, Y.; Wang, H.; Wu, J.; Zhao, R.; Lu, Y.; Xin, B. Controlled Facile Synthesis and Photocatalytic Activity of Ultrafine High Crystallinity TiO_2 Nanocrystals with Tunable Anatase/Rutile Ratios. *Appl. Surf. Sci.* **2014**, *294*, 36−41.
(55) Pei, C.; Leung, W. Enhanced Photocatalytic Activity of Electrospun TiO_2/ZnO Nanofibers with Optimal Anatase/Rutile Ratio. *Catal. Commun.* **2013**, *37*, 100−104.
(56) Liu, J.; Ge, Q. A Precursor State for Formation of $TiAl_3$ Complex in Reversible Hydrogen Desorption/Adsorption from Ti-Doped $NaAlH_4$. *Chem. Commun.* **2006**, *6*, 1822−1824.
(57) Tian, N.; Zhou, Z.; Sun, S.; Ding, Y.; Wang, Z. Synthesis of Tetrahexahedral Platinum Nanocrystals with High-Index Facets and High Electro-Oxidation Activity. *Science* **2007**, *316*, 732−735.

DOI: 10.1021/acsami.6b13973
ACS Appl. Mater. Interfaces XXXX, XXX, XXX−XXX